

See discussions, stats, and author profiles for this publication at: <https://www.researchgate.net/publication/231630797>

# Exciton–Vibrational Relaxation and Transient Absorption Dynamics in LH1 of *Rhodopseudomonas viridis*: A Redfield Theory Approach

ARTICLE in THE JOURNAL OF PHYSICAL CHEMISTRY B · MAY 2002

Impact Factor: 3.3 · DOI: 10.1021/jp012048k

---

CITATIONS

42

---

READS

26

2 AUTHORS, INCLUDING:



Rienk van Grondelle

VU University Amsterdam

647 PUBLICATIONS 23,660 CITATIONS

SEE PROFILE

# Exciton–Vibrational Relaxation and Transient Absorption Dynamics in LH1 of *Rhodopseudomonas viridis*: A Redfield Theory Approach

Vladimir Novoderezhkin<sup>†</sup> and Rienk van Grondelle<sup>\*,‡</sup>

A. N. Belozersky Institute of Physico-Chemical Biology, Moscow State University, Moscow 119899, Russia,  
and Department of Biophysics, Faculty of Sciences, Vrije Universiteit, De Boelelaan 1081,  
1081 HV Amsterdam, The Netherlands

Received: May 30, 2001; In Final Form: January 10, 2002

We explain the ultrafast transient absorption (TA) dynamics in the core LH1 antenna of *Rhodopseudomonas viridis* at 77 K (Monshouwer, R.; Baltuška, A.; van Mourik, F.; van Grondelle, R. *J. Phys. Chem. A* **1998**, *102*, 4360) using a disordered exciton model with strong coupling to two vibrational modes and weak coupling of vibrational and electronic coordinates to the thermal bath. A quantitative fit of the excitation wavelength-dependent TA dynamics was obtained using the density matrix equation with the Redfield relaxation operator. The sequential and coherent contributions to the TA dynamics were analyzed separately. The time-dependent red shift of TA was explained in terms of exciton relaxation. The lifetimes of higher exciton states of 12–75 fs (depending on the state) were determined from the fit.

## Introduction

Excitation energy transfer via molecular excitons is the basic mechanism of photosynthetic light-harvesting, which allows for ultrafast cascading from higher- to lower-energy states together with an effective energy migration in antenna and energy delivery to the reaction center.<sup>1,2</sup> The discovery of the high-resolution structure of two bacterial antennae<sup>3,4</sup> has resulted in major advances in our understanding of the nature of the electronic excited states and their role in the energy-transfer dynamics.<sup>5</sup> Direct observation of the dynamics (including initial relaxation of delocalized exciton states and migration of the quasi-steady-state exciton wave packet) of this process is possible from transient absorption (TA) studies via a picosecond/femtosecond pump–probe technique. Such measurements have revealed initial ultrafast (sub-100 fs) equilibration in the ring-like aggregates of LH1/LH2 antenna followed by slower dynamics.<sup>6–18</sup> Understanding the physical origins of this initial fast dynamics process together with a quantitative explanation of the experimental data is a challenging problem that has not yet been solved.

It is now well established that excitonic interactions together with energetic disorder in antenna complexes of purple bacteria result in a nonhomogeneous electronic structure of the absorption band, as was manifested for the first time by the change of fluorescence polarization upon tuning a narrow-band excitation source over the major  $Q_y$  band.<sup>19–21</sup> Fast relaxation/migration in such a system gives rise to specific TA dynamics that is typical for aggregated antenna pigments but is absent in isolated dimeric subunits and monomers. This behavior was demonstrated for the first time by Visser et al.,<sup>7</sup> who compared the isotropic TA dynamics for LH1 of *Rhodospirillum rubrum* with

those of both the dimeric B820 subunit of the LH1 antenna and the bacteriochlorophyll (BChl) monomers. In LH1, they found pronounced TA dynamics (12-nm red shift of the isosbestic point and 8-nm red shift of the bleaching peak) reflecting a fast exciton equilibration, whereas no red-shift dynamics was found in either the lowest-state absorption band of the dimeric subunit or for monomeric BChl. These results were explained in terms of ultrafast hopping of localized excitations. A similar dynamic red shift of about 20 nm (explained in terms of exciton relaxation) was observed in LH1 of *Rhodobacter capsulatus*.<sup>6</sup> However, the time resolution in both these experiments (200–400 fs) was not high enough to allow for a precise estimation of the relaxation (or hopping) time constant.

A 35-fs pump–probe study of LH2 of *Rhodobacter sphaeroides* showed relaxation components in the 10–100-fs range.<sup>9</sup> A 40–50-fs one-color study of LH1 and LH2 antenna of *Rb. sphaeroides* gave a 50–60-fs isotropic component, whereas tuning the wavelength to the blue resulted in the appearance of short-lived (<20-fs) components.<sup>14</sup> It is difficult, however, to draw any conclusions about the nature of these components because the excitation and probing carried out with such short pulses has no spectral selectivity. To obtain TA dynamics that would directly reflect the exciton equilibration under selective excitation and probing, two-color experiments with longer pulses are needed.

Two-color experiments were performed for LH2 of *Rb. sphaeroides* with 70-fs pulses at low temperature<sup>16</sup> and with 65-fs pulses at room temperature.<sup>10</sup> In both cases, excitation either on the blue or red side of the B850 band was applied. Upon blue excitation, the TA spectrum showed a dynamic red shift of 3–5 nm with a time constant of 80–110 fs at room temperature<sup>10</sup> and a dynamic red shift of 4 nm with a time constant of 100 fs at low temperature.<sup>16</sup> In both cases, the shift was almost absent upon red excitation. The authors explained

\* To whom correspondence should be addressed. E-mail: rienk@nat.vu.nl.  
Fax: 31-20-4447899.

<sup>†</sup> Moscow State University.

<sup>‡</sup> Vrije Universiteit.

that this phenomenon was caused by relaxation from higher exciton states that were initially excited by the short-wavelength pump.

A similar two-color experiment was carried out with 100-fs pulses for LH1 of *Rhodospseudomonas viridis*.<sup>15</sup> Upon blue-side excitation, a dynamic red shift was observed with a time constant of 130–150 fs. The amplitude of this shift (15–20 nm) is several times larger than that of LH2 and is similar to that obtained for other LH1 antennae in earlier experiments.<sup>6,7</sup> Upon tuning the excitation wavelength to the middle of the band, the dynamic red shift becomes less pronounced.

Besides this ultrafast red shift, more long-lived oscillatory features were observed for LH1 of *Rps. viridis* because of coupling of electronic excitations to two vibrational modes with frequencies (depending on temperature) of 48–65 and 103–108 cm<sup>-1</sup>.<sup>15</sup> In a preceding paper,<sup>22</sup> we have explained these oscillatory features within the limits of the disordered exciton model for LH1 antenna. We have obtained a quantitative fit of the TA dynamics using the doorway–window picture in the vibrational eigenstate basis. To model long-lived vibrational coherence in the 200 fs to 2 ps range, we neglected the exciton relaxation dynamics by assuming that exciton equilibration is complete at 200–300 fs. Here we generalize this model by taking into account the coupled exciton–vibrational dynamics at short delays using Redfield relaxation theory.<sup>23</sup> At these delays (i.e., <200 fs), the TA dynamics is determined mostly by a large dynamic red shift due to fast exciton relaxation superimposed upon relatively weak oscillatory features, which are due to vibrational coherences. Here our goal is to explain the nonoscillatory part of the experimental TA dynamics that occur on a femtosecond time scale to gain insight into the exciton relaxation phenomena in photosynthetic antenna systems.

### Theoretical Model

The system Hamiltonian in the eigenstate basis is

$$H = \sum_a \omega_g^a |g, a\rangle \langle g, a| + \sum_{k,b} \omega_k^b |k, b\rangle \langle k, b| + \sum_{q,f} \omega_q^f |q, f\rangle \langle q, f| \quad (1)$$

where  $\omega_g^a$ ,  $\omega_k^b$ , and  $\omega_q^f$  are the energies of the states  $(g, a)$ ,  $(k, b)$ , and  $(q, f)$ . The indexes  $g$ ,  $k$ , and  $q$  denote the ground-, one-, and two-exciton eigenstates;  $a$ ,  $b$ , and  $f$  stand for vibronic sublevels of these states. The interaction with the laser field is described by

$$H_E = -\mathbf{E}(t) \left[ \sum_{k,a,b} \mathbf{d}_{kg}^{ba} |k, b\rangle \langle g, a| + \sum_{k,q,b,f} \mathbf{d}_{qk}^{fb} |q, f\rangle \langle k, b| \right] + \text{h.c.}$$

$$\mathbf{E}(t) = \mathbf{E}_1(\omega_1, t) + \mathbf{E}_2(\omega_2, t) + \text{c.c.}$$

$$\mathbf{E}_1(\omega_1, t) = \mathbf{e}_1 \epsilon_1(t) e^{-i\omega_1 t + i\mathbf{k}_1 \mathbf{r}}$$

$$\mathbf{E}_2(\omega_2, \tau, t) = \mathbf{e}_2 \epsilon_2(t - \tau) e^{-i\omega_2 t + i\mathbf{k}_2 \mathbf{r}} \quad (2)$$

where  $\mathbf{d}_{kg}^{ba}$  and  $\mathbf{d}_{qk}^{fb}$  are the dipole moments for the  $(g, a) \rightarrow (k, b)$  and  $(k, b) \rightarrow (q, f)$  transitions. The external field is represented by the pump and probe optical pulses with frequencies of  $\omega_1$  and  $\omega_2$ , wavevectors  $\mathbf{k}_1$  and  $\mathbf{k}_2$ , polarization vectors  $\mathbf{e}_1$  and  $\mathbf{e}_2$ , and envelopes  $\epsilon_1(t)$  and  $\epsilon_2(t - \tau)$ , respectively ( $\epsilon_1$  and  $\epsilon_2$  can be complex in the case of frequency modulated pulses). The delay between pump and probe pulses is  $\tau$ .

The pump–probe signal is given by<sup>24</sup>

$$\Delta A(\omega_1, \omega_2, \tau) =$$

$$2\omega_2 \int_{-\infty}^{\infty} dt \text{Im}\{\mathbf{E}_2^*(\omega_2, \tau, t) \mathbf{P}^{(3)}(\omega_1, \omega_2, \tau, t)\}$$

$$\mathbf{P}^{(3)}(\omega_1, \omega_2, \tau, t) =$$

$$e^{-i\omega_2 t + i\mathbf{k}_2 \mathbf{r}} \left\{ \sum_{k,a,b} \mathbf{d}_{kg}^{ab} \rho_{kg}^{ba(3)}(\omega_2) + \sum_{k,q,b,f} \mathbf{d}_{qk}^{bf} \rho_{qk}^{fb(3)}(\omega_2) \right\} \quad (3)$$

where  $\mathbf{P}^{(3)}$  denotes the nonlinear (third-order) polarization that is determined by the reduced density matrix  $\rho^{(3)}$  in third order with respect to the external field. The polarization should oscillate at frequency  $\omega_2$  to contribute to the pump–probe signal. Correspondingly, only the  $\rho^{(3)}$  elements oscillating at frequency  $\omega_2$  have to be taken into account. The slowly varying amplitudes of these elements are denoted as  $\rho_{kg}^{ba(3)}(\omega_2)$  and  $\rho_{qk}^{fb(3)}(\omega_2)$ . These amplitudes, which are dependent on  $\omega_1$ ,  $\omega_2$ ,  $\mathbf{e}_1$ ,  $\mathbf{e}_2$ ,  $\tau$ , and  $t$ , can be obtained from the Liouville equation for the reduced density matrix  $\rho$

$$\frac{d\rho}{dt} = -i[H + H_E, \rho] - R\rho \quad (4)$$

$R$  is the Redfield superoperator describing the relaxation in the limit of weak coupling of the electronic and vibrational coordinates with the thermal bath.<sup>23,25</sup> The system–bath interaction in the site representation is taken to be

$$V = \sum_j f_g^j Q^j |g\rangle \langle g| + \sum_{j,n} (F_n + f_n^j (Q^j - \Delta_n^j)) |n\rangle \langle n| \quad (5)$$

where  $|n\rangle$  is the wave function corresponding to excitation of the  $n$ -th molecule in the aggregate;  $f_g^j$ ,  $f_n^j$ , and  $F_n$  are bath-induced fluctuations responsible for vibrational relaxation of the  $j$ -th mode in the ground and excited state and for electronic relaxation, respectively. The coupling is linear in the vibrational coordinate  $Q^j$  measured from the minimum of the ground-state surface. Displacement of the excited-state surface of the  $n$ -th site (in the  $Q^j$  direction) is  $\Delta_n^j$ . We suppose that

$$\langle f_n^j f_m^j \rangle = \delta_{ij} \delta_{nm} \alpha^j \quad \langle f_g^j f_g^j \rangle = \delta_{ij} \alpha^j \quad \langle f_g^j f_n^j \rangle = 0 \quad (6a)$$

$$\langle F_n F_m \rangle = \delta_{nm} \beta \quad \langle f_g^j F_n \rangle = 0 \quad \langle f_n^j F_m \rangle = 0 \quad (6b)$$

The first equality in eq 6a indicates that fluctuations that induce vibrational relaxation for different sites or for different vibrational modes are uncorrelated. The fluctuations acting on different vibrational modes of the ground state and on vibrations within the ground- and excited-state manifolds are uncorrelated as well (second and third equalities in eq 6a, respectively). There is no correlation between fluctuations that induce electronic and vibrational relaxation (last two equalities in eq 6b) or between fluctuations acting on different electronic excited sites (so that the electronic relaxation is described by the model of uncorrelated diagonal dynamic disorder (see first equality in eq 6b)). The light-harvesting antenna consists of many ( $N = 32$  for LH1) pigment–protein subunits, each containing a huge number (several thousands) of atoms. It is reasonable to suppose that individual pigments have their own thermal bath represented by many degrees of freedom, thus giving rise to uncorrelated fluctuations acting on the electronic and nuclear coordinates of different sites. Electronic and nuclear coordinates of the same site also interact with different uncorrelated degrees of freedom. This assumption is corroborated by the fact that electronic and nuclear relaxation dynamics have different (by 1–2 orders) time scales and by the fact that electronic relaxation does not destroy

the vibrational coherence.<sup>22</sup> A possible correlation between the bath coupled to the same nuclear mode in the ground and excited states of the same site would not influence the ground- and excited-state dynamics but can influence the ground- to excited-state coherences (and, therefore, the spectral width of the exciton–vibrational lines). In our model, however, these coherences (and the corresponding line widths) are determined mostly by fast electronic dephasing rather than by slow vibrational equilibration so that they are relatively insensitive to the particular choice of the vibrational relaxation model, which is why we used the simplest model of uncorrelated ground- and excited-state vibrational dynamics (the third term of eq 6a). Generalization to the case of off-diagonal disorder, intersite, intermode, exciton–vibrational correlations, and nonlinear Q coupling is straightforward.

We note that the same relaxation model was used in our previous paper<sup>22</sup> and allowed us to explain quantitatively the vibrational dynamics for delays larger than those on the exciton relaxation time scale (i.e., the  $F_n$  fluctuations were not taken into consideration). Here we generalize this model by introducing the electronic relaxation into the interaction Hamiltonian (eq 5) to explain the coupled exciton–vibrational dynamics for arbitrary time delays including the ultrafast exciton equilibration within 100–200 fs after impulsive excitation. As in the previous study, we assume that the displacements are site-independent (i.e.,  $\Delta_n^i = \Delta^i$ ), which implies that the displacements of the one- and two-exciton eigenstates  $|k\rangle$  and  $|q\rangle$  are  $\Delta^i$  and  $2\Delta^i$ , respectively<sup>22</sup> (i.e., the displacements do not depend on  $k$  and  $q$ ). Generally, an electronic excitation in the antenna is created with a nonuniform change in the equilibrium positions of nuclear coordinates (i.e., the oscillator displacement of a nuclear mode depends on the site number  $n$ , thus reflecting a nonuniform lattice deformation due to polaron effects). In the case of moderate electron–phonon coupling, one can neglect the effects of polaron formation and consider the lattice deformation to be uniform. Such an approximation (used in our previous paper; see ref 22 for more details) is reasonable if the polaron is large enough, for example, when the polaron-induced length is larger than the disorder-induced length of the exciton wave functions. In this case (and also because of the uncorrelated character of excitonic and vibrational relaxation), the Redfield superoperator splits into two parts that describe the relaxation of the electronic and vibrational subsystems separately.

The expansion of eq 4 up to third order in the eigenstate representation is given in Appendix A. The corresponding components of the Redfield tensor are derived in Appendix B.

The nonlinear absorption calculated according to eq 3 and eqs A1–A8 should be averaged over the realizations of the static disorder—random shifts of the site energies and intermolecular couplings that will perturb the energies and dipole strengths in the eigenstate representation (i.e., the  $\omega_k^b$ ,  $\omega_q^f$ ,  $\mathbf{d}_{kg}^{ba}$ , and  $\mathbf{d}_{qk}^{fb}$  values). The disorder of the vibrational parameters can also be considered and may require an additional averaging step. Finally, an average should be made over the different orientations that the antenna units have with respect to the polarizations of the pump/probe fields (see Appendix C).

### Model of the Antenna

As in our previous papers,<sup>22,26</sup> we assume that the pigment arrangement in the core antenna of *Rps. viridis* is analogous to that of LH2 of the BChl *a*-containing bacteria. As a model of the antenna, we consider a circular aggregate of  $N = 24$  or 32 BChl *b* molecules with either  $C_{12}$  or  $C_{16}$  symmetry (the elementary unit cell contains two BChl *b* molecules that are

bound to the  $\alpha$  and  $\beta$  polypeptides). The orientations of the two BChls in a dimeric unit cell and the Mg–Mg distances between BChls are approximately the same as those for the strongly coupled B850 ring of BChl *a* molecules in the LH2 antenna from *Rps. acidophila*.<sup>3</sup> We consider the BChl *b* species to two-level molecules. The interaction energies between BChl *b* molecules are  $M_{12} = 400 \text{ cm}^{-1}$ ,  $M_{23} = 290 \text{ cm}^{-1}$ ,  $M_{13} = -52 \text{ cm}^{-1}$ , and  $M_{14} = 14 \text{ cm}^{-1}$  where  $M_{12}$  corresponds to the intradimer interactions,  $M_{23}$ , to interdimer nearest-neighbor interactions,  $M_{13}$ , to second-nearest-neighbor interactions, and  $M_{14}$ , to third-nearest-neighbor interactions. The unperturbed  $Q_y$  electronic transition energies of the two BChls in a dimeric unit cell are  $E_1$  and  $E_2$  (with  $E_1 - E_2 = 300 \text{ cm}^{-1}$ ).<sup>27,28</sup> The site inhomogeneity of the LH1 antenna was described by uncorrelated perturbations  $\delta E$  to  $E_1$  and  $E_2$ . The inhomogeneous width (fwhm of the Gaussian distribution of  $\delta E$  values) is  $\sigma$ . Alternative models with correlated disorder, elliptic deformation of the ring, and breaking of the closed ring by removing a few dimeric subunits were analyzed as well.

We assume that the electronic transitions are coupled to two vibrational modes with frequencies of  $\Omega_1 = 58 \text{ cm}^{-1}$  and  $\Omega_2 = 110 \text{ cm}^{-1}$ , Huang–Rhys factors  $S_1 = 0.41$  and  $S_2 = 0.23$ , and relaxation constants (rates for the  $1 \rightarrow 0$  vibronic transition)  $\gamma_1 = 11 \text{ cm}^{-1}$  and  $\gamma_2 = 11 \text{ cm}^{-1}$  at 77 K.<sup>22</sup> These relaxation constants were fixed by an appropriate choice of  $\alpha$  and  $\tau_c$  values in eq B5 so that the vibrational part of the Redfield tensor can be calculated using eq B3.

The excitonic Redfield tensor depends on the wave function amplitudes  $c_n^k$  and  $c_{nm}^d$  (eq B2) and the exciton splitting values  $\omega_{kk'}$  (eq B6), which can be obtained by diagonalization of the one- and two-exciton Hamiltonians (for each particular realization of the static disorder). The relaxation rates between pairs of levels with different splittings are determined by the spectral density  $W^2 \exp(-W)$  where  $W = \omega_{kk'}/\omega_c$  and  $\omega_c$  is the characteristic frequency (see eq B6) that we varied in our study from 15 to  $150 \text{ cm}^{-1}$  (i.e., around the  $50 \text{ cm}^{-1}$  value suggested for LH1/2 antenna).<sup>29</sup> The coupling parameter  $\chi$  that determines the amplitude of the site energy modulation that is necessary to explain the experimental relaxation dynamics is about  $300\text{--}600 \text{ cm}^{-1}$ . It follows from eqs B2 and B6 that the electronic relaxation rates increase proportionally to  $\chi$ . The pure dephasing of the exciton states is determined by the constant  $\Gamma$  (eq B6). For example, the pure dephasing of one-exciton states is given by the difference between the whole line width  $2R_{kkgk}$  and the relaxation-induced broadening  $R_{kkkk}$ . According to eqs B2 and B6, this difference is equal to  $\sum_n (c_n^k)^4 2\text{Re}(J_{kk})$ . In our simplest model, the spectral density  $J_{kk'}$  falls to zero if  $\omega_{kk'} = 0$ , so we introduced (following ref 29) an additional parameter to account for pure dephasing (i.e.,  $J_{kk} = \Gamma/2$ ). Notice that by using more complicated spectral densities (see for example eq B8) one can obtain the pure dephasing constant from  $2\text{Re}(J_{kk'})$  at  $k = k'$ , but we found out that the actual value of the pure dephasing is not critical in our model, where the line shapes are determined mostly by relaxation-induced broadening (for higher states) or inhomogeneous broadening (for the lowest state). We have varied the  $\Gamma$  value over the  $40\text{--}160 \text{ cm}^{-1}$  range that can be roughly estimated from the absorption line shape (see discussion below).

The pump and probe pulses were assumed to be Gaussian with a fwhm of 100 fs. The probe wavelength was tuned from 990 to 1090 nm both for 1017- and 1036-nm excitation corresponding to the blue side and the maximum of the absorption spectrum at 77 K, respectively.<sup>15</sup>



## Numerical Calculations

The nonlinear transient absorption spectra were averaged over 500–2000 realizations of the disorder using a Monte Carlo procedure. The time evolution of the density matrix was calculated using the basis of the 9 lowest one-exciton states and the 60 lowest two-exciton states with 8 vibronic sublevels each. If we consider exciton states without vibrational structure, then eqs A1–A8 can be solved directly, including all relaxation terms (i.e., with the full Redfield tensor) and all contributions (sequential, non-time-ordered, and coherent). However, the inclusion of vibronic states greatly complicates numerical simulations, so we have to make some assumptions to simplify the problem to make it solvable.

First, we use the secular approximation for the vibrational and exciton parts of the Redfield tensor, which implies that only the resonant terms  $R_{ijkl}$  with  $\omega_{ij} = \omega_{kl}$  are taken into account (such as the population relaxation  $R_{iikk}$ , the coherence decay  $R_{ijij}$ , and the coherence transfer  $R_{ijij'}$  with  $\omega_{ij} = \omega_{i'j'}$ ). The coherence transfer is important in the description of the vibrational dynamics of a harmonic oscillator<sup>30</sup> and must be taken into account for a quantitative fit of the vibrational coherences in the LH1 antenna.<sup>22</sup> On the other hand, the electronic coherence transfer in the antenna can be neglected because of the strong anharmonicity of the exciton levels.<sup>29,31</sup> Here we neglect the transfer of electronic coherences within the one-exciton manifold as well as the transfer of coherences between the ground state and the one- or two-exciton states, which means that the relaxation matrix in eqs A1, A6, A7, and A8 becomes diagonal and we have independent (noncoupled) equations containing only the decay of coherences. A solution of the third-order equations (eqs A7 and A8) can then be obtained in integral form with a subsequent summation over  $k$  and  $q$  (in  $\mathbf{P}^{(3)}$  in eq 3) inside the integrand. In cases in which the dynamics of the second-order populations and coherences is much slower than the dephasing of the third-order polarization (i.e., the pulse spectrum is narrower than the whole width of the SE, PB, or ESA bands), the integration can be done only for the fast dephasing factor, giving a sum of Lorentzian factors (for the individual exciton transitions) describing a dispersion of the slowly varying polarization amplitude. This stationary polarization limit reduces the whole set of equations to second-order equations.

We have calculated the nonoscillatory part of the kinetics, thus neglecting terms  $\rho_{kk}^{bb'}(0)$  and  $\rho_{gg}^{aa'}(0)$  with  $b \neq b'$  and  $a \neq a'$ . The terms  $\rho_{kk}^{bb'}(0)$  with different  $k$  and  $k'$  values give rise to an aperiodic decay rather than to oscillations because the splitting between  $k$  and  $k'$  states is less than the line width of these states (see below). We retain these terms, but their contribution was found to be relatively small. Much more significant are the non-time-ordered terms  $\rho_{kk'}^{bb'}(\omega_2 - \omega_1)$  describing the coherence between exciton–vibronic states created by overlapping pump and probe. If the difference frequency is in resonance with any pair of states (i.e.,  $\omega_2 - \omega_1 = \omega_{kk'}^{bb'}$ ), then the coherence between these states will be much larger than that created by the pump pulse alone.

## Results

**Dynamics of Transient Absorption.** The model presented above allows us to obtain a good quantitative fit of the experimental data including absorption and pump–probe (transient absorption) spectra for the core antenna of *Rps. viridis* at 77 K.<sup>15</sup> Figure 1 shows a simultaneous fit of the absorption and TA spectra for two different excitation wavelengths

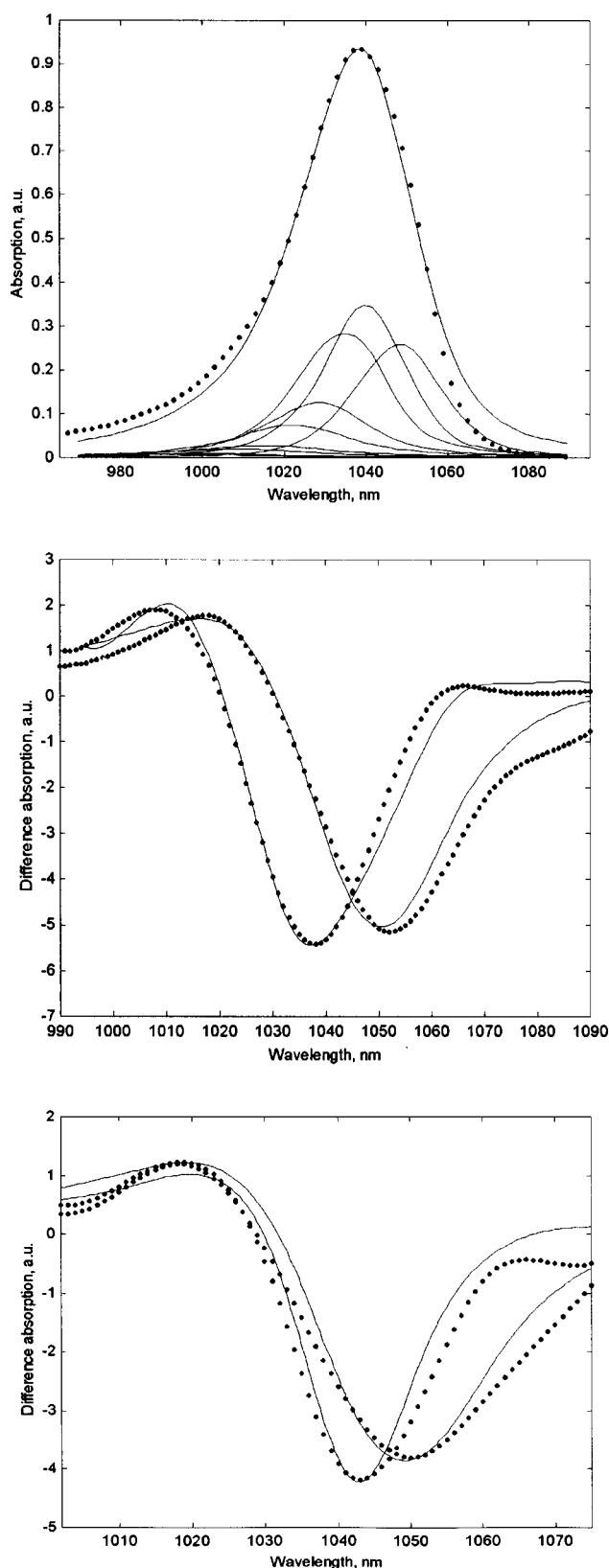


**Figure 1.** Simultaneous fit of linear absorption (top frame) and pump–probe profiles upon 1017 nm excitation (middle frame) and 1036 nm excitation (bottom frame) at 77 K. Pump–probe spectra are shown at 0 and 400 fs delay for both excitation wavelengths (increase in time delay corresponds to a red-shift of the spectra). Experimental data is shown by points, calculated spectra – by solid lines. The calculated absorption spectrum is shown together with contributions of the individual exciton components.  $N=32$ , the site inhomogeneity is  $\sigma=575$   $\text{cm}^{-1}$ , the coupling parameter  $\chi=490$   $\text{cm}^{-1}$ , the pure dephasing parameter  $\Gamma=70$   $\text{cm}^{-1}$ , and the characteristic frequency  $\omega_c=75$   $\text{cm}^{-1}$ .

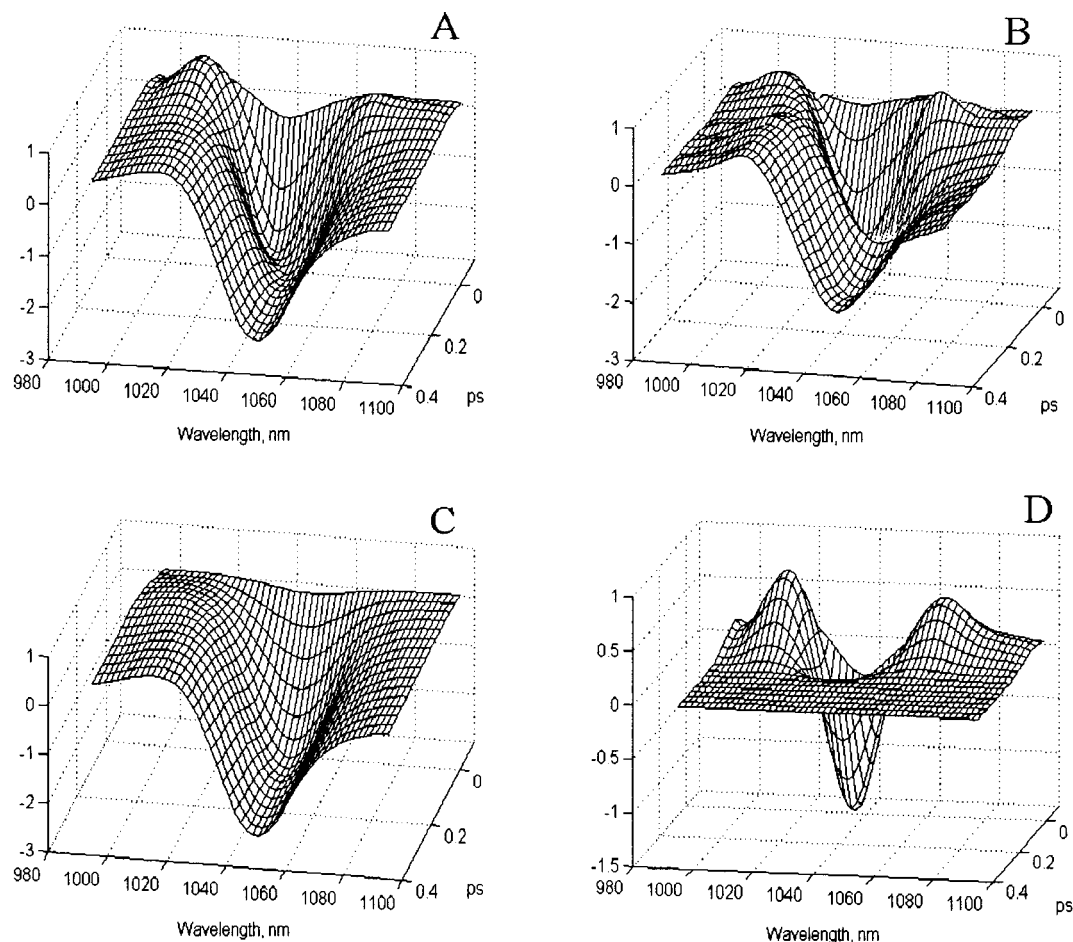


**Figure 2.** The calculated (A) and measured (B) transient absorption  $\Delta A$  as a function of probe wavelength and time delay upon 1017 nm excitation. Sequential  $\Delta A_S$  (C) and coherent  $\Delta A_C$  (D) parts of the calculated  $\Delta A$  signal are shown as well. Parameters are the same as in Figure 1. A wavelength step of 2 nm and a time delay step of 33.3 fs were used to plot the three-dimensional surfaces corresponding to the calculated and measured data.

corresponding to the blue side and the middle of the 77 K absorption band (1017 and 1036 nm, respectively). For each excitation wavelength, we have modeled the dynamics of the isotropic (magic angle) TA spectra. The best fit was obtained for  $N = 32$ , the site inhomogeneity value  $\sigma = 575 \text{ cm}^{-1}$ , the coupling parameter  $\chi = 490 \text{ cm}^{-1}$ , the pure dephasing parameter  $\Gamma = 70 \text{ cm}^{-1}$ , and the characteristic frequency  $\omega_c = 75 \text{ cm}^{-1}$ . In Figure 1, we present the TA spectra (both measured and calculated) at a 0-fs delay corresponding to the moment of maximal pump–probe overlap and at a 400-fs delay when the exciton relaxation is complete. Upon blue-side excitation, the experimental spectrum exhibits an 11-nm shift of the ESA maximum, a 10-nm shift of the isosbestic point, and a 15-nm shift of the bleaching maximum. Upon middle-band excitation, there is no shift of the ESA maximum and isosbestic point, whereas the bleaching peak shifts to the red by 7 nm. These values are reproduced by the model with an accuracy of about 2 nm (Figure 1).

A more detailed picture of the TA dynamics upon blue excitation (1017 nm) is presented in Figures 2 and 3. Figure 2 shows a 3-D view of the calculated (A) and measured (B) spectra at detection wavelengths from 990 to 1090 nm and time delays from  $-100$  fs to 400 fs. The sequential  $\Delta A_S$  (C) and coherent  $\Delta A_C$  (D) parts of the calculated  $\Delta A$  signal are shown separately. Figure 3 shows the frontal view of the same surfaces (i.e., spectral profiles for different delays are superimposed). It is clearly seen from Figure 3 that both calculated and measured spectra become undistinguishable at 200–230-fs delays, indicat-

ing that the exciton relaxation is complete. During the relaxation period (i.e., between  $-100$  and 230 fs), the TA dynamics is determined by the interplay of the time-dependent  $\Delta A_S$  and  $\Delta A_C$  spectra. These two contributions reflecting the relaxation dynamics and coherent artifacts cannot be directly obtained from the measured spectra, but they follow separately in the model.

The sequential signal  $\Delta A_S$  (Figures 2C and 3C) grows during the pump pulse, reaches its maximum at 130 fs, and shows some decrease of bleaching amplitude between 130 and 230 fs. Because of the relaxation, the bleaching peak of  $\Delta A_S$  continuously shifts from 1044 to 1050 nm for  $-100$ - to 230-fs delays. The coherent signal  $\Delta A_C$  (Figures 2D and 3D) shows a blue-shifted negative peak at 1036 nm and two positive maxima. The amplitude of the coherent signal is maximal near zero delay. As a result, we have a blue-shifted bleaching and two (long- and short-wavelength) absorption maxima of the total signal  $\Delta A$  near zero delay (Figure 3A). After a 50-fs delay, the long-wavelength maximum disappears, whereas the short-wavelength maximum transforms to a broader and a more highly red-shifted sequential ESA maximum. After 130 fs, the coherent contribution completely disappears, and at the same time, the sequential signal reaches its maximum. The combined action of sequential and coherent contributions results in the very large apparent Stokes shift of the total signal at delays from  $-100$  to 230 fs. Thus, the bleaching peak of the calculated  $\Delta A$  spectrum shifts from 1036 to 1050 nm (Figure 3A).

The model calculations clearly unravel the origins of the experimental spectra (Figure 3B). The latter show dynamic

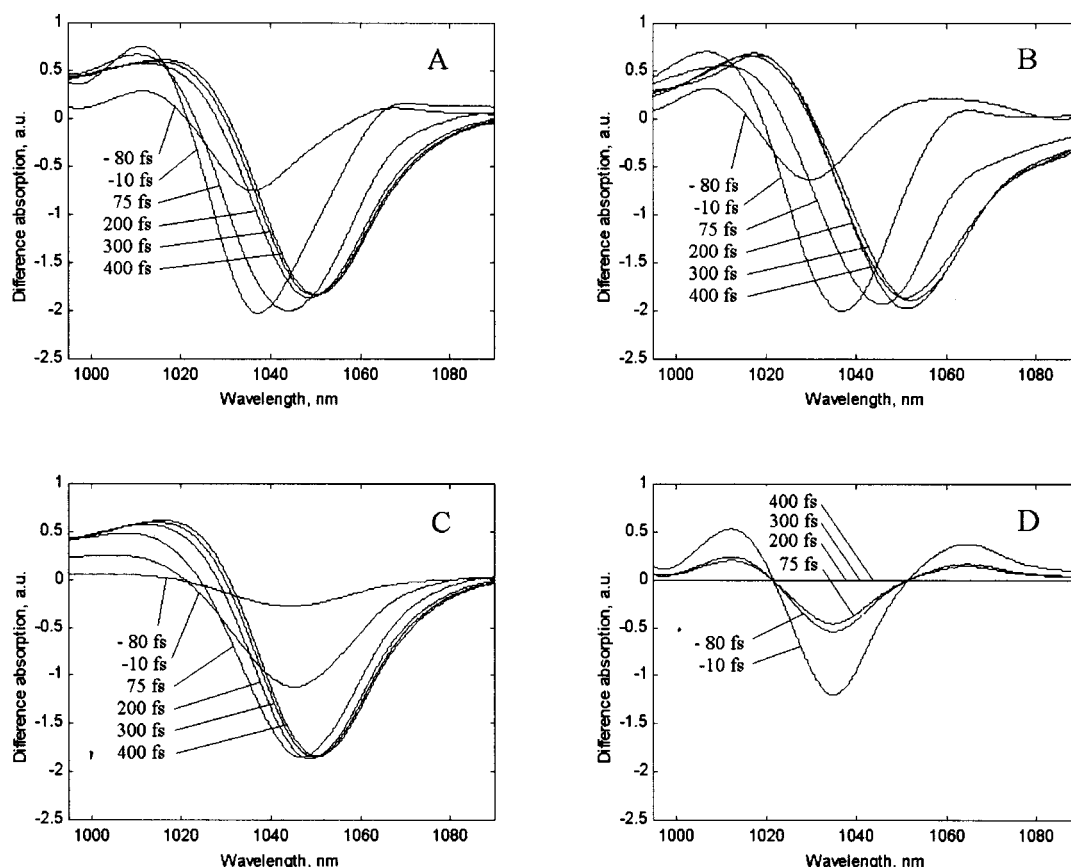


**Figure 3.** The same as in Figure 2, but in frontal view, i.e., spectral profiles for delays of  $-80$ ,  $-10$ ,  $75$ ,  $200$ ,  $300$ , and  $400$  fs.

features that are very similar to the modeled ones. Notice, however, that the measured dynamics is more complicated because of oscillatory features, which were neglected in our modeling. Because of vibrational oscillations, the dynamic red shift is accompanied by modulations of the bleaching amplitude.

An unexplained feature in the experimental spectra is an additional shift of the bleaching peak at negative time delays. In the model, there is very little red shift between the  $-100$ - to  $0$ -fs delay, whereas the measured bleaching peak shifts by  $6$  nm in this time interval. Such a shift cannot be connected with vibrational oscillations, which were neglected in our modeling, because its time scale (dozens of fs) is faster than the oscillatory period and its amplitude is bigger than modulations of the TA amplitude because of vibrational coherences. In ref 32, an ultrafast (sub-50-fs) red shift of the TA spectra with a similar amplitude was obtained for the B820 subunit of LH1. This phenomenon was ascribed to self-trapping due to fast phonon dynamics.<sup>32</sup> To verify this possibility, we need to include in the model strong coupling to a manifold of phonon modes with a spectral density spread over a wide range of frequencies (this coupling is not present in our current model). Alternatively, these features may be ascribed to experimental artifacts such as residual frequency modulation of the pulses<sup>33</sup> or other factors that give rise to specific features in TA dynamics at negative time delays.<sup>10</sup>

Notice that for larger delays (from  $400$  fs to  $2$  ps) the calculated and measured spectra show no additional spectral evolution such as a further red shift or some changes in line shape (data not shown). The vibrational coherence still exists up to  $1.5$ – $2$  ps, thus giving rise to some oscillations in bleaching peak position (within  $1$ – $2$  nm) and in bleaching amplitude (within  $\pm 5\%$  of this amplitude), but vibrational population dynamics gives only a very small contribution (less than  $1$  nm)

to the dynamic red shift. It is clear (and can be verified) that the TA shifting during the first  $100$ – $200$  fs is determined mostly by the exciton relaxation.

Upon middle-band excitation, there is no pronounced red-shift dynamics of the sequential signal, so the TA evolution is determined mostly by the coherent contribution (data not shown). The latter has a negative peak at  $1043$  nm, giving rise to the  $\Delta A$  shifting from  $1043$  to  $1050$  nm (as shown in Figure 1, bottom frame).

**Electronic Relaxation Parameters.** The parameters that determine the exciton relaxation dynamics (free parameters in our fitting) are the site inhomogeneity  $\sigma$ , the coupling parameter  $\chi$  (that determines the amplitude of the bath-induced dynamic disorder), the characteristic frequency of the system–bath coupling  $\omega_c$ , and the electronic pure dephasing  $\Gamma$ . These parameters also determine the line broadening due to coupling of the electronic coordinate to the slow and fast bath dynamics (inhomogeneous and homogeneous broadening). An additional line-broadening (or line nonhomogeneity) factor is the vibronic substructure of each of the exciton levels, which was determined in a previous paper<sup>22</sup> and is fixed in our present analysis.

The site inhomogeneity value  $\sigma$  was determined from the fit with an accuracy of  $\pm 5\%$ . An increase (decrease) in  $\sigma$  results in absorption and TA spectra that are too broad (narrow). In the earlier study,<sup>26</sup> the  $\sigma$  value was estimated (from a simultaneous fit of absorption and steady-state TA spectra) to be  $440$  and  $545$   $\text{cm}^{-1}$  for antenna sizes of  $N = 24$  and  $32$ , respectively. Both these sizes were used for modeling of LH1 in our previous work.<sup>22,26</sup> Notice that such a difference in antenna size is not critical for the fit if one keeps the inhomogeneous width of the exciton levels constant. The latter is equal (approximately) to  $\sigma/\sqrt{N}$ , which is why we need different values of  $\sigma$  using different  $N$ . The present fit of the time-dependent TA gave an

inhomogeneity value of  $575 \text{ cm}^{-1}$  for  $N = 32$ , which is close to the earlier estimation.

Alternatively, the absorption line width can be explained by using much smaller disorder values together with the introduction of some amount of correlated energy shift or ring deformation, both giving rise to additional splitting between the  $k = \pm 1$  levels.<sup>34–36</sup> We concluded that these models fail to explain the low-temperature fluorescence polarization of LH1,<sup>37</sup> thus giving a negative polarization in the middle of the band because of the presence of weakly overlapping  $k = \pm 1$  levels with perpendicular transition dipoles. These models also cannot explain the dynamics of transient absorption. From our analysis, it follows that the measured TA dynamics upon blue-side excitation reflects a relaxation from higher  $k = \pm 2$  and  $\pm 3$  levels. We also have seen that upon middle-band excitation corresponding to excitation of the  $k = \pm 1$  levels the red-shift dynamics is much less pronounced (Figure 1). In the models with elliptical deformations, the absorption spectrum is determined mostly by the  $k = \pm 1$  states, whereas the higher exciton states specify that the  $k = \pm 2$  states remain forbidden. In this case, the model calculation demonstrate that the red-shift dynamics upon blue excitation is almost the same as for middle-band excitation in contradiction with the experiment (see Figure 1). To correctly reproduce the short-wavelength excitation dynamics (Figure 1, middle frame), transitions to the higher exciton states must determine the blue wing of the linear absorption spectrum, which is the case for the disordered ring model.

The coupling parameter  $\chi$  can be determined with an accuracy of  $\pm 10\%$ . Any alteration of this value results in proportional changes in all relaxation rates and all homogeneous line widths. It can be shown<sup>25</sup> that Redfield theory is applicable if the relaxation times are not too short (i.e., if the bath-induced fluctuations acting on the system eigenstates do not exceed the thermal energy  $k_B T$ , where  $k_B$  is the Boltzmann constant and  $T$  is the temperature). In the case of uncorrelated diagonal coupling (i.e., the fluctuations of the different site energies are uncorrelated), the fluctuation amplitude in the eigenstate representation  $\chi_{\text{eig}}$  would be related to the coupling parameter (amplitude of the site energy modulation)  $\chi$  through the fourth power of the wave function amplitude (see Appendix B). The latter is equal to the participation ratio, which is about 0.1 for the higher exciton states in our model.<sup>22,26</sup> In our model, the coupling parameter in the site representation required to explain the experimental relaxation dynamics is  $\chi = 490 \text{ cm}^{-1}$ . Thus, the fluctuations that induce relaxation from the higher states are relatively weak in the eigenstate representation; consequently, the Redfield approximation is valid (at room temperature and even lower temperatures up to 77 K).

An important parameter is the characteristic frequency  $\omega_c$  that determines the pathways of exciton relaxation. The strongest connection is between levels whose splitting corresponds to the peak of the spectral density distribution,  $W^2 \exp(-W)$ , where  $W = \omega_{kk'}/\omega_c$  (eq B6). The relaxation rate is maximal if  $\omega_{kk'} = 2\omega_c$ . At low  $\omega_c$  values ( $15\text{--}35 \text{ cm}^{-1}$  for our  $N$  and  $\sigma$ ), relaxation occurs only between nearest-neighbor levels, and for intermediate values ( $50\text{--}80 \text{ cm}^{-1}$ ), the maximal rate corresponds to relaxation to the second- or third-nearest neighbors among one-exciton states. For larger  $\omega_c$  values, the levels from different sides of the absorption will have the highest rate of exchange (note that the uphill transfer between well-separated states is forbidden at 77 K because of the Boltzmann factor in eq B6). The best fit of the experimentally observed relaxation dynamics was obtained for  $\omega_c = 75 \text{ cm}^{-1}$ . The corresponding time

**TABLE 1: Relaxation Rates of the One-Exciton Populations Averaged over Disorder  $\langle R_{\text{ppkk}} \rangle$ , the Corresponding Time Constants  $\langle R_{\text{ppkk}} \rangle^{-1}$ , and the Electronic Dephasing between Ground and One-Exciton States  $\langle 2R_{\text{kgk'g}} \rangle^a$**

$\langle R_{\text{ppkk}} \rangle^{-1}$ , fs						
<b>254</b>	−121	−84	−63	−71	−91	−138
−662	<b>75</b>	−154	−66	−58	−58	−80
−772	−602	<b>41</b>	−129	−62	−46	−57
−1359	−494	−453	<b>23</b>	−156	−51	−49
−3356	−990	−456	−553	<b>17</b>	−86	−52
−13 906	−3158	−926	−419	−311	<b>12</b>	−134
−58 158	−11 260	−3222	−992	−460	−511	<b>12</b>
$\langle R_{\text{ppkk}} \rangle$ , $\text{cm}^{-1}$						
<b>20.8</b>	−43.9	−63.4	−83.7	−74.3	−58.4	−38.3
−8.0	<b>71.0</b>	−34.5	−80.3	−91.2	−91.2	−66.6
−6.8	−8.8	<b>128.7</b>	−41.0	−85.1	−114.6	−92.6
−3.9	−10.7	−11.7	<b>232.7</b>	−33.9	−104.6	−109.3
−1.5	−5.3	−11.6	−9.5	<b>313.2</b>	−61.7	−101.8
−0.3	−1.6	−5.7	−12.6	−17.0	<b>441.2</b>	−39.6
−0.0	−0.4	−1.6	−5.3	−11.5	−10.3	<b>448.5</b>
$\langle 2R_{\text{kgk'g}} \rangle$ , $\text{cm}^{-1}$						
<b>38.8</b>	0	0	0	0	0	0
0	<b>84.7</b>	0	0	0	0	0
0	0	<b>139.5</b>	0	0	0	0
0	0	0	<b>242.1</b>	0	0	0
0	0	0	0	<b>323.0</b>	0	0
0	0	0	0	0	<b>448.5</b>	0
0	0	0	0	0	0	<b>455.1</b>
$\langle 2R_{\text{kgk'g}} \rangle - \langle R_{\text{kkkk}} \rangle$ , $\text{cm}^{-1}$						
<b>18.0</b>	<b>13.7</b>	<b>10.8</b>	<b>9.4</b>	<b>8.8</b>	<b>7.3</b>	<b>6.6</b>

<sup>a</sup> Off-diagonal terms in the  $k$ th column correspond to the  $k \rightarrow p$  transitions; diagonal terms correspond to the lifetime of the  $k$ th state (the exciton states are arranged in increasing order of energy). The  $R_{\text{kgk'g}}$  tensor is diagonal in our model; the  $2R_{\text{kgk'g}}$  value is the homogeneous line width (fwhm); the difference  $2R_{\text{kgk'g}} - R_{\text{kkkk}}$  corresponds to a pure dephasing (this difference is equal to  $\Gamma$  multiplied by a participation ratio of the  $k$ th exciton state – see eq B2).

constants of population relaxation are listed in Table 1. The downhill transfer times between pairs of levels lie in the 50–150 fs range. The lifetime of the  $k$ -th level decreases rapidly with  $k$ . The lifetimes of the higher states (12–20 fs for  $k = \pm 2, \pm 3$ ) are significantly shorter than the pulse duration (100 fs), but we cannot use shorter pulses to see this fast relaxation because under broad-band excitation it would be impossible to excite these higher levels selectively.

The value of the pure dephasing constant  $\Gamma$  is not critical for our fit. The real pure dephasing of the  $k$ -th level is  $\Gamma$  multiplied by the participation ratio  $\sum_n \langle n^2 \rangle_k$  (eq B2). The latter is about 0.1 for the higher levels (i.e., the widths of higher levels are mostly determined by their lifetimes rather than by pure dephasing). However, the value of  $\Gamma$  can have a significant effect on the shape of the spectrum of the lowest  $k = 0$  level (which is not broadened because of relaxation and which has a participation ratio of about 0.2–0.25), increasing the red wing of the absorption (Figure 1). We then conclude that  $\Gamma$  should be not larger than  $50\text{--}70 \text{ cm}^{-1}$  at 77 K (the corresponding value of the pure dephasing is  $5\text{--}18 \text{ cm}^{-1}$ ), whereas a lower limit cannot be estimated. The contributions of relaxation and pure dephasing to the homogeneous line width are given in Table 1. Notice that the difference  $2R_{\text{kgk'g}} - R_{\text{kkkk}}$  corresponding to the pure dephasing of the  $k$ -th exciton state is about  $0.25\Gamma$  for the lowest state and decreases to  $0.1\Gamma$  for the higher states (Table 1), as was expected from the participation ratio of about 0.25–0.1 calculated for the LH1 antenna.<sup>26</sup> Notice, furthermore, that the pure dephasing of the lowest state is  $18 \text{ cm}^{-1}$  at 77 K in our model, whereas  $4 \text{ cm}^{-1}$  was obtained at 4 K by hole-burning



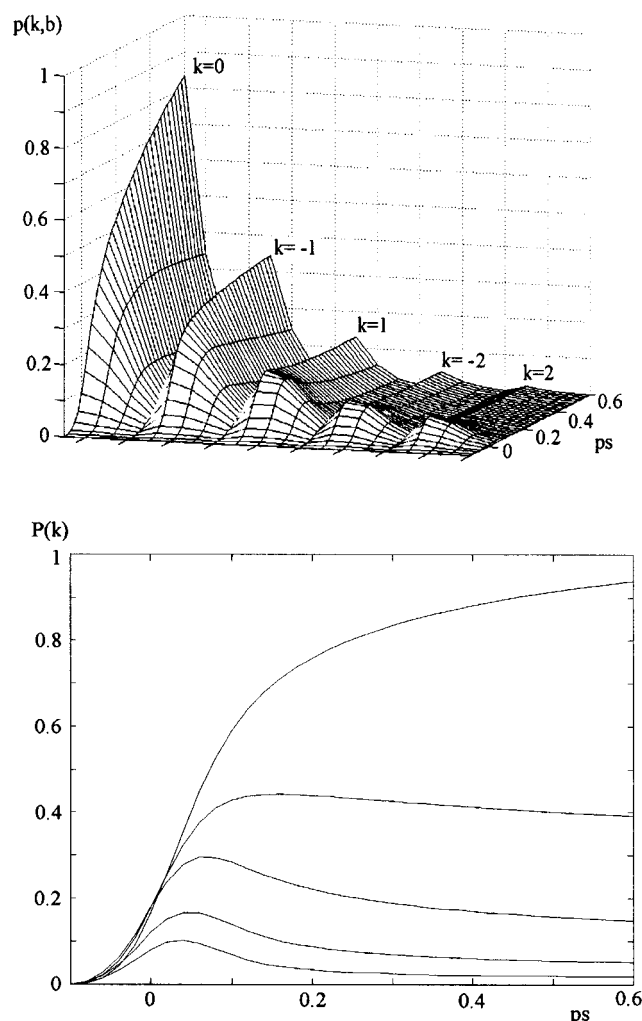


**Figure 4.** Time-dependent populations  $p(k,b)$  of exciton-vibrational states corresponding to five lowest exciton states ( $k = 0, \pm 1$ , and  $\pm 2$ ) with 4 lowest vibronic sublevels each upon blue excitation (1017 nm) at 77 K (top) and exciton populations  $P(k)$  for  $k = 0, \pm 1$ , and  $\pm 2$  (bottom). Parameters are the same as in Figure 1.  $k = 0, k = -1, k = 1, k = -2$ , and  $k = 2$  label the zero phonon origin of each of five exciton states shown in the top frame.

studies of LH1.<sup>45</sup> Such a difference looks reasonable when bearing in mind that  $\Gamma$  typically increases with temperature.

The dynamics of the populations of the exciton-vibrational states  $p(k,b)$  is given by the diagonal elements of the one-exciton density matrix (eq A2). The kinetics of the populations  $p(k,b)$  of the five lowest exciton levels and their four lowest vibronic sublevels (upon blue excitation) are shown in Figure 4 (top frame) together with the exciton populations  $P(k)$  calculated by taking the trace over the vibrational states (bottom frame). The Figure shows the very fast relaxation of the higher exciton levels ( $k = \pm 2$ ) together with the slower equilibration among the lower levels ( $k = 0, \pm 1$ ). This fast relaxation of the higher states is responsible for the dynamic red shift of the TA spectrum between a -100- and 230-fs delay upon blue excitation. Interestingly, the slow redistribution of the excitation density between the three lowest exciton levels for delays larger than 230 fs (which is clearly seen in Figure 4) is not accompanied by any spectral shifts (in the case of the blue excitation shown in Figure 3). Upon middle-band excitation, the higher states are not populated, whereas the dynamics of the three lowest states does not lead to any pronounced red-shift dynamics. So, we conclude again that the experimentally observed red-shift

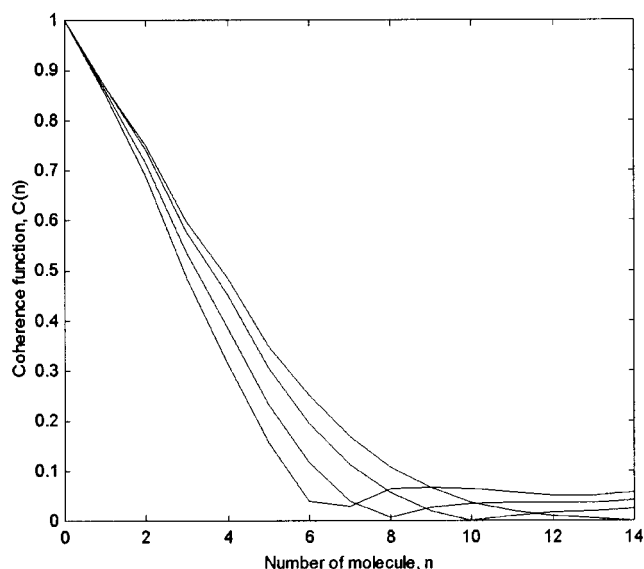


**Figure 5.** Coherence function  $C(n)$  for time delays (from left to right) -80, 0, 80, 400 fs. Absolute values of  $C(n)$  normalized to unity for each time delay are shown. Parameters are the same as in Figure 1. The steady-state coherence length (fwhm)- 8 BChls.

dynamics is mostly determined by the presence of strongly allowed higher exciton states ( $k = \pm 2$ ) predicted by the disordered exciton model.

The calculated dynamics of the exciton-vibrational populations also shows some vibrational equilibration within the exciton states (Figure 4, top frame). For example, the population of the zero phonon level of the second exciton state,  $p(k = -1, b = 0)$ , increases because of relaxation from higher vibronic sublevels (see the decrease in  $p(k = -1, b = 1)$ ), whereas the total population of this exciton component is decreasing. The population of the zero phonon sublevel of the third exciton component  $p(k = +1, b = 0)$  displays a fast decrease immediately after the pump because of exciton relaxation, but at larger delays, it becomes almost time-independent because of vibrational relaxation from higher vibrational states that compensates the depopulation of the whole exciton state. It is interesting that this process of slow but nonnegligible dynamics of vibrational populations between 0- and 600-fs delays gives only a weak contribution to the red-shift dynamics in this time scale.

The dynamics of exciton states within the one-exciton manifold effectively results in a time evolution of the exciton wave packet in real space. Coherent properties of the exciton wave packet created by the pump can be described by a coherence function, which is defined as

$$C(n) = \langle \sum_{b,m} \rho_{m,m+n}^{bb(2)}(0) \rangle = \langle \sum_{b,m} \sum_{k,k'} c_m^k c_{m+n}^{k'} \rho_{kk'}^{bb(2)}(0) \rangle \quad (7)$$

The time evolution of  $C(n)$  is shown in Figure 5. Initially, the pump creates a nonequilibrium superposition of exciton states. Some (relatively small) part of the excitation density is delocalized over the whole antenna, but the largest part of the initial wave packet is localized only on a few (in our calculation, about six molecules (fwhm of  $C(n)$ )). Because of exciton relaxation, the delocalized part (the wing of the  $C(n)$  function) disappears with a time constant of about 80 fs. The resulting steady-state coherence function has a width of eight molecules at 77 K in agreement with our earlier modeling.<sup>26</sup> The steady-state delocalization length at 77 K exceeds the initial length because only the lowest state (with an admixture of 20–30%

of the next higher state) is populated in equilibrium. In contrast, at room temperature we would have a further dynamic localization of the excitation with a steady-state coherence length of 4–5 molecules.<sup>14,26,29,38</sup>

## Discussion

**Origins of Ultrafast Spectral Dynamics. 1. Exciton Relaxation.** Excitation of higher exciton states results in a blue-shifted stimulated emission (SE) and a broad excited-state absorption (ESA) component that is determined by transitions from higher one-exciton states to the two-exciton manifold (the dipole strength of these transitions is spread over a large number of two-exciton levels). After exciton relaxation, the SE is shifted to the red, and the ESA becomes narrower and also more red-shifted (because only transitions for a few of the lowest two-exciton states are allowed from the lower one-exciton levels). As a result, the total TA spectrum (i.e., the sum of SE, ESA, and a nonshifting photobleaching (PB)) exhibits a large time-dependent red-shift reflecting the exciton relaxation dynamics.

**2. Long-Lived Vibrational Relaxation.** Short-wavelength excitation can also be followed by the relaxation of higher vibration states that induces a red shift of the SE and a blue shift of the ESA components for each of the exciton states. Both shifts have a time constant of  $\gamma^{-1}$  (where  $\gamma$  is the vibrational relaxation constant) and are superimposed with oscillatory features in the case of underdamped modes (i.e.,  $\gamma \ll \Omega$ ). This is the case for the 58- and 110-cm<sup>-1</sup> modes with Huang–Rhys factors of  $S_1 = 0.41$  and  $S_2 = 0.23$  and a relaxation constant of 11 cm<sup>-1</sup> observed in LH1 of *Rps. viridis* at 77 K. For  $S \ll 1$ , the nonoscillatory part of the SE and ESA shifts produces some changes in the wings of the corresponding spectral components, whereas the maximum (determined mostly by the zero phonon line) remains unshifted. Combinations of these shifts for SE and ESA together with the unshifted PB result in a relatively weak shift of the total TA signal, as was observed experimentally<sup>15</sup> and explained theoretically in a previous paper.<sup>22</sup>

**3. Phonon-Induced Shift.** The spectral density of electron–phonon coupling may contain a few sharp peaks (with  $\gamma \ll \Omega$ ) corresponding to underdamped modes as well as a broad, low-frequency wing (with  $\gamma_{\text{ph}} > \Omega$  where  $\gamma_{\text{ph}}$  is the relaxation constant of phonons) determined by superimposed overdamped phonon modes. If these modes are strongly coupled to the electron coordinate, they should be included in the modeling as additional system coordinates. The equilibration of these phonon modes results in a nonoscillatory aperiodic spectral shift with a time constant of  $(\gamma_{\text{ph}})^{-1}$  that may be comparable or even shorter than the time scale of exciton relaxation. Such a phenomena (with the sub-50 fs time scale) was suggested to occur for the B820 subunit<sup>32</sup> and is generally assumed to explain the ultrafast decay of the peak shift in three-pulse photon echo experiments on LH1 and LH2.<sup>39–41</sup>

**4. Slow Equilibration.** There may also be some slower components of the dynamic red-shift, thus reflecting some energy migration or relaxation along the nuclear coordinate, which represents a slow reorganization of the environment.<sup>8,17</sup>

According to the present study, the greatest part of the dynamic red shift of the TA in the sub-picosecond time scale can be explained by the pure exciton relaxation within the one-exciton manifold of the LH1. Notice that in this model we neglected a possible contribution from the ultrafast phonon equilibration.

**Exciton Relaxation and Line Broadening.** The model presented here implies a strong inhomogeneity of the antenna (i.e., the  $\sigma/M$  ratio is about 1.4–1.5). However, the inhomogeneous

width of the exciton levels,  $\sigma/\sqrt{N} \approx 100$  cm<sup>-1</sup>, is less than the homogeneous broadening of the higher levels because of exciton relaxation (100–450 cm<sup>-1</sup>, see Table 1). The latter is determined by the coupling parameter  $\chi = 490$  cm<sup>-1</sup> and the pure dephasing parameter  $\Gamma = 70$  cm<sup>-1</sup>. In principle, the steady-state spectra can be modeled using an alternative parameter set with higher  $\sigma/M$  and lower  $\chi$  and  $\Gamma$  values. For example, Kühn and Sundström<sup>29</sup> explained the steady-state pump–probe spectrum for LH2 by assuming that  $\sigma/M = 2.3$ ,  $\chi = 50$ –100 cm<sup>-1</sup>, and  $\Gamma = 5$ –20 cm<sup>-1</sup>. In this case, the inhomogeneous width is much larger than the homogeneous broadening because of slower exciton relaxation. Consequently, this model predicted slow dynamics of the transient absorption with a time constant of 0.5–1 ps,<sup>29</sup> whereas the true dynamics is 1 order of magnitude faster, thereby giving a complete exciton relaxation within 200–300 fs for LH1<sup>15</sup> and LH2 antennae.<sup>10,16</sup> To explain such a fast equilibration of the electronic subsystem, we need higher values of  $\chi$  and  $\Gamma$ . These higher values do not qualitatively change the exciton dynamics but reduce its time scale. For example, the dynamics of the coherence function (Figure 5) looks very similar to that obtained in ref 29, but in the latter case, the delocalized wing of  $C(n)$  disappears with a time constant of 600–700 fs, whereas in our model the corresponding time constant is about 80 fs.

**Coherent Artifact and Dynamic Stokes Shift.** We have seen (Figures 2 and 3) that because of overlap in the timing of pump and probe laser pulses there is an additional coherent contribution to the TA spectra that is shifted to the blue and that has its maximum at zero time delay. As a result, the TA spectra will display an additional dynamic red shift that can be even more pronounced than the “true” red shift because of exciton relaxation (which is viewed as a red shift of the sequential contribution). The time dependence of the coherent contribution in the stationary polarization limit is  $\exp(-\tau^2/(\tau_1^2 + \tau_2^2))$  if the pump and probe intensities are  $\exp(-t^2/\tau_1^2)$  and  $\exp(-(t - \tau)^2/\tau_2^2)$  where  $\tau_1$  and  $\tau_2$  are the pump and probe pulse durations, respectively, and  $\tau$  is the pump–probe delay. This means that the characteristic time of the “coherent” red shift is about  $\sqrt{2}$  times larger than the pulse duration. It is interesting to note that all experimental observations of the transient absorption shift reported so far revealed a main component with a time constant of about  $\sqrt{2}$  times the length of the pulses used. Thus, the main component of the dynamic red shift is 130–150 fs for LH1 probed by 100-fs pulses,<sup>15</sup> 100 fs for LH2 at low temperature measured with 70-fs pulses,<sup>16</sup> and 80–100 fs for LH2 at room temperature measured with 65-fs pulses.<sup>10</sup> It seems very likely that the red-shift dynamics in all these cases is strongly dominated by the coherent factor, whereas the true relaxation rates are shorter than the pulse duration, lying in the 10–80 fs range according to our analysis. Notice that components shorter than 50 fs were observed for LH1 and LH2.<sup>9,10,14</sup> It was also found that a shift of the excitation wavelength to the blue resulted in more short-lived decays up to sub-20-fs components upon excitation at the extreme blue edge of the absorption band.<sup>14</sup> Unfortunately, in most cases, these true relaxation components are always hidden under a slow-pulse envelope, whereas shorter pulses cannot be used for selective excitation of higher exciton levels because of the relatively small splitting between levels in combination with their large widths. We remind the reader that upon nonselective excitation/probing with very short pulses decay components up to 10 fs were observed, but they cannot be assigned to any particular pair of levels.<sup>9</sup> Direct visualization of exciton relaxation (including coherent oscillations) is possible only for a system with large

(compared with the line broadening) splitting, such as the B820 dimer<sup>32</sup> or the BChl dimer of the reaction center.<sup>42</sup> On the other hand, the relaxation rates for more complicated systems such as LH1/LH2 can be obtained by global analysis of the data on the basis of an appropriate relaxation theory (such as Redfield theory).

**Fitting of Spectral Shapes: Limitations of Redfield Theory.** Redfield theory is a unified approach that allows us to obtain a self-consistent description of spectral line shapes and relaxation dynamics of coupled electronic and nuclear coordinates of the system. In particular, we were able to explain quantitatively the amplitude and time scale of the dynamic red shift of the TA spectra associated with exciton relaxation in the LH1 antenna of *Rps. viridis*. Let us now discuss some aspects of our fitting of the experimental spectra that are connected with the limitations of Redfield theory.

Redfield theory predicts an exponential decay of electronic coherences as a result of weak coupling to the thermal bath. Therefore, we obtain a superposition of Lorentzian line shapes in the absorption profile (Figure 1, top frame) that clearly contains more intensity at the red side than at the experimental red wing. Figure 1 also shows that the calculated red wing is broader than the red wing of the lowest exciton level (the latter is determined by an inhomogeneous width of about  $\sigma/\sqrt{N} = 100 \text{ cm}^{-1}$  and a pure dephasing value of  $18 \text{ cm}^{-1}$ ; see Table 1). It therefore follows that the calculated red wing is determined by the superposition of Lorentzian wings from higher exciton states that are significantly broadened from fast relaxation. This result is an artifact of Redfield theory, yielding Lorentzian lines with broad overlapping wings, whereas the real line shapes are probably closer to Gaussian. For example, the polarized fluorescence of LH1 will be negative upon red excitation when calculated with Lorentzian line shapes (because of contributions from the wings of higher exciton states) but becomes positive (with the values close to the experimental values) when Gaussian shapes are used.<sup>37</sup> Another example is the shape of the TA oscillations in LH1 upon red excitation that cannot be reproduced with Lorentzian line shapes but can be fitted quantitatively with Voigt profiles that are close to pure Gaussians.<sup>22</sup> A more realistic line shape (introduced phenomenologically in refs 22 and 37) can be obtained from a more sophisticated theory that includes strong coupling to the bath, but this approach is beyond the limit of the present study that is based on the Redfield approach. Notice, however, that the above-mentioned line shape artifact is critical only for the modeling of nonlinear phenomena upon red excitation. In the case of blue and middle-band excitation (modeled in the present work), the calculated TA dynamics are not very sensitive to the line shape.

Another limitation of Redfield theory is connected with the eigenstate representation for the system coordinates (electronic and nuclear). As a result, the number of nuclear modes that is strongly coupled to electronic excitations is limited to one or two. The remaining part of the nuclear coordinates is considered to be a bath that is weakly coupled to the system coordinates, which makes it difficult to obtain realistic models of the blue wing of the absorption, the Stokes shift, and the red wing of the stimulated emission. This is the reason for the systematic deviation of the calculated TA profiles from the measured profiles. Thus, the negative red wing in the PB/SE region is always narrower than the experimental red wings in all pump-probe simulations for LH1/LH2 that have been performed.<sup>10,14,22,26,29,38,44</sup> This red-side fit can be improved by taking into account the strong coupling to two vibrational modes for LH1,<sup>22</sup> but the improved fit is still not perfect. Notice that

in all these simulations only the steady-state TA spectra (with respect to exciton relaxation) were modeled. The only exception is ref 10, where the dynamic red shift of the TA in LH2 is calculated. In this model, a qualitative explanation of the red shift was obtained, but the calculated amplitude of this shift was found to be several times lower than the experimental value.<sup>10</sup> In this respect, a quantitative explanation of the amplitude and time scale of the red shift of TA in our present paper is remarkable. We believe that the remaining discrepancies of our fit (some deviation of simulated and measured data, unclear behavior at negative delays etc.) are due to limitations of our present model. We hope to overcome these limitations at the next level of approximation.

## Conclusions

We have modeled the ultrafast transient absorption dynamics in the core LH1 antenna of *Rps. viridis* at 77 K using a disordered exciton model with strong coupling to two vibrational modes and weak coupling of the vibrational and electronic coordinates to the thermal bath. The time-dependent red shift of TA can be quantitatively explained in terms of exciton relaxation in the one-exciton manifold. The lifetimes of the higher exciton states of 12–75 fs (depending on the state) were determined from a fit of the experimental data. We conclude that the experimentally observed red-shift dynamics is mostly determined by the presence of strongly allowed higher exciton states ( $k = \pm 2$ ) that is predicted by the disordered exciton model. The dynamics of vibrational populations gives a relatively weak contribution to the total red-shift dynamics. An overlap in time of pump and probe laser pulses gives rise to an additional dynamic red shift that can be even more pronounced than the true red shift because of exciton relaxation.

**Acknowledgment.** V.N. was supported by a visitor's grant from the Dutch Foundation of Scientific Research (NWO), by the Russian–Dutch Research Cooperation Program, and by the Russian Foundation for Basic Research, Grant No. 02-04-48779. This research was supported by the Foundation of Earth and Life Sciences (ALW), which is part of the Dutch Foundation of Scientific Research and the Human Frontiers in Science Program, Grant No. 1932802.

## Appendix A

We use the following notations:  $\rho_{kg}^{ba}$  is the density matrix element corresponding to the coherence between the (g, a) and (k, b) states ( $\rho_{kk}^{bb'}$ ,  $\rho_{gg}^{aa}$ ,  $\rho_{gg}^{fa}$ , and  $\rho_{qk}^{fb}$  are defined similarly).  $\rho^{(n)}$  denotes the density matrix of the n-th order with respect to the external field.  $\rho_{kg}^{ba}(\omega)$  denotes the slowly varying amplitude of the matrix element oscillating with frequency  $\omega$  (i.e.,  $\rho_{kg}^{ba} = \rho_{kg}^{ba}(\omega) \exp(-i\omega t)$ ). In the rotating wave approximation (RWA), these are the elements with  $\omega = \pm\omega_1$  and  $\pm\omega_2$  in first-order,  $\omega = 0$ ,  $\omega_2 - \omega_1$ , and  $\omega_2 + \omega_1$  in second-order, and  $\omega = \omega_2$  in third-order expansions.

In first order, the  $\mathbf{E}_{1,2}$  or  $\mathbf{E}_{1,2}^*$  fields create coherences between the ground and one-exciton states,  $\rho_{kg}^{ba}(\omega_{1,2})$  or  $\rho_{gk}^{ab}(-\omega_{1,2})$ , respectively:

$$\left[ \frac{d}{dt} + i(\omega_{kg}^{ba} - \omega_{1,2}) \right] \rho_{kg}^{ba(1)}(\omega_{1,2}) = -[R\rho^{(1)}(\omega_{1,2})]_{kg}^{ba} + i\epsilon_{1,2}(\mathbf{e}_{1,2} \mathbf{d}_{kg}^{ba})\rho_{gg}^{aa(0)} \\ \rho_{gk}^{ab(1)}(-\omega_{1,2}) = (\rho_{kg}^{ba(1)}(\omega_{1,2}))^* \quad \rho_{gg}^{aa(0)} = P_a \quad (A1)$$



where  $P_a$  is the steady-state population of the vibronic levels in the ground state. The decay of the ground- to one-exciton coherences is described by the action of the Redfield operator on  $\rho^{(1)}$ . Generally, the relaxation term  $R\rho^{(1)}$  is nondiagonal, thus including coherence transfer processes (see Appendix B).

In second order, the  $\mathbf{E}_1^*\mathbf{E}_1$  and  $\mathbf{E}_1\mathbf{E}_1^*$  interactions may create a particle in the excited state  $\rho_{kk'}^{bb'}(0)$  or a hole in the ground state  $\rho_{gg}^{aa'}(0)$ :

$$\left[\frac{d}{dt} + i\omega_{kk'}^{bb'}\right]\rho_{kk'}^{bb'(2)}(0) = -[R\rho^{(2)}(0)]_{kk'}^{bb'} + i\epsilon_1 \sum_a (\mathbf{e}_1 \mathbf{d}_{kg}^{ba}) \rho_{gk'}^{ab(1)}(-\omega_1) - i\epsilon_1^* \sum_a \rho_{kg}^{ba(1)}(\omega_1) (\mathbf{e}_1 \mathbf{d}_{gk}^{ab'}) \quad (\text{A2})$$

$$\left[\frac{d}{dt} + i\omega_{gg}^{aa'}\right]\rho_{gg}^{aa'(2)}(0) = -[R\rho^{(2)}(0)]_{gg}^{aa'} + i\epsilon_1^* \sum_{k,b} (\mathbf{e}_1 \mathbf{d}_{gk}^{ab}) \rho_{kg}^{ba(1)}(\omega_1) - i\epsilon_1 \sum_{k,b} \rho_{gk}^{ab(1)}(-\omega_1) (\mathbf{e}_1 \mathbf{d}_{kg}^{ba'}) \quad (\text{A3})$$

where  $\omega_{kk'}^{bb'} = \omega_k^b - \omega_{k'}^{b'}$ . Notice that the excited state is in fact a superposition of exciton–vibrational states, thus including coherences between one-exciton states as well as vibrational coherences, so the excited-state dynamics is determined by the coupled motion of the exciton and vibrational wave packets, whereas the ground-state hole is just a vibrational wave packet. Dynamics of exciton and vibrational relaxation is described by the action of the Redfield operator on  $\rho^{(2)}$ .

For time delays corresponding to the overlap of the pump and probe pulses, there exist additional  $\mathbf{E}_1^*\mathbf{E}_2$  and  $\mathbf{E}_2\mathbf{E}_1^*$  interactions that create populations  $\rho_{kk'}^{bb'}(\omega_2 - \omega_1)$  and  $\rho_{gg}^{aa'}(\omega_2 - \omega_1)$  that oscillate with a difference frequency of  $\omega_2 - \omega_1$

$$\left[\frac{d}{dt} + i(\omega_{kk'}^{bb'} - \omega_2 + \omega_1)\right]\rho_{kk'}^{bb'(2)}(\omega_2 - \omega_1) = -[R\rho^{(2)}(\omega_2 - \omega_1)]_{kk'}^{bb'} + i\epsilon_2 \sum_a (\mathbf{e}_2 \mathbf{d}_{kg}^{ba}) \rho_{gk'}^{ab(1)}(-\omega_1) - i\epsilon_1^* \sum_a \rho_{kg}^{ba(1)}(\omega_2) (\mathbf{e}_1 \mathbf{d}_{gk}^{ab'}) \quad (\text{A4})$$

$$\left[\frac{d}{dt} + i(\omega_{gg}^{aa'} - \omega_2 + \omega_1)\right]\rho_{gg}^{aa'(2)}(\omega_2 - \omega_1) = -[R\rho^{(2)}(\omega_2 - \omega_1)]_{gg}^{aa'} + i\epsilon_1^* \sum_{k,b} (\mathbf{e}_1 \mathbf{d}_{gk}^{ab}) \rho_{kg}^{ba(1)}(\omega_2) - i\epsilon_2 \sum_{k,b} \rho_{gk}^{ab(1)}(-\omega_1) (\mathbf{e}_2 \mathbf{d}_{kg}^{ba'}) \quad (\text{A5})$$

as well as the  $\mathbf{E}_1\mathbf{E}_2$  and  $\mathbf{E}_2\mathbf{E}_1$  interactions, thus creating coherence between the ground and two-exciton states  $\rho_{qg}^{fa}(\omega_2 + \omega_1)$ :

$$\left[\frac{d}{dt} + i(\omega_{qg}^{fa} - \omega_2 - \omega_1)\right]\rho_{qg}^{fa(2)}(\omega_2 + \omega_1) = -[R\rho^{(2)}(\omega_2 + \omega_1)]_{qg}^{fa} + i\epsilon_2 \sum_{k,b} (\mathbf{e}_2 \mathbf{d}_{qk}^{fb}) \rho_{kg}^{ba(1)}(\omega_1) + i\epsilon_1 \sum_{k,b} (\mathbf{e}_1 \mathbf{d}_{qk}^{fb}) \rho_{kg}^{ba(1)}(\omega_2) \quad (\text{A6})$$

In third-order we have three types of contributions (in the rotating wave approximation). The  $\mathbf{E}_2(\mathbf{E}_1^*\mathbf{E}_1 + \mathbf{E}_1\mathbf{E}_1^*)$  interactions correspond to a sequential (i.e., time-ordered) pump–probe. In this case, the pump acts first by creating an excited-state

population and a ground-state hole, which gives rise to the absorption changes that consist of excited-state absorption (ESA1), stimulated emission (SE1), and ground-state photobleaching (PB1). The  $\mathbf{E}_1(\mathbf{E}_1^*\mathbf{E}_2 + \mathbf{E}_1^*\mathbf{E}_2)$  interactions correspond to a non-time-ordered signal where the electronic population and bleaching are created by overlapping pump and probe. The corresponding absorption changes will be denoted as ESA2, SE2, and PB2. Finally, the  $\mathbf{E}_1^*(\mathbf{E}_1\mathbf{E}_2 + \mathbf{E}_1\mathbf{E}_2)$  terms correspond to pathways where ground to two-exciton coherences are created by overlapping pump and probe. The third interaction then creates the  $\rho_{qk}^{fb}(\omega_2)$  or  $\rho_{kg}^{ba}(\omega_2)$  coherences, which give rise to the so-called coherent artifact. We will denote these two contributions as CA' or CA'', respectively. (Usually, the term “coherent artifact” refers to all nonsequential contributions—the sum of ESA2, SE2, PB2, CA', and CA''). Alternatively, it denotes the pathways with no electronic population—CA' and CA''). The third-order density matrix elements are then given by

$$\left[\frac{d}{dt} + i(\omega_{qk}^{fb} - \omega_2)\right]\rho_{qk}^{fb(3)}(\omega_2) = -[R\rho^{(3)}(\omega_2)]_{qk}^{fb} - i\epsilon_1^* \sum_a \rho_{qg}^{fa(2)}(\omega_1 + \omega_2) (\mathbf{e}_1 \mathbf{d}_{gk}^{ab}) + i\epsilon_2 \sum_{k',b'} (\mathbf{e}_2 \mathbf{d}_{qk'}^{fb'}) \rho_{k'k}^{b'b(2)}(0) + i\epsilon_1 \sum_{k',b'} (\mathbf{e}_1 \mathbf{d}_{qk'}^{fb'}) \rho_{k'k}^{b'b(2)}(\omega_2 - \omega_1) \quad (\text{A7})$$

$$\left[\frac{d}{dt} + i(\omega_{kg}^{ba} - \omega_2)\right]\rho_{kg}^{ba(3)}(\omega_2) = -[R\rho^{(3)}(\omega_2)]_{kg}^{ba} + i\epsilon_1^* \sum_{q,f} (\mathbf{e}_1 \mathbf{d}_{kq}^{bf}) \rho_{qg}^{fa(2)}(\omega_1 + \omega_2) - i\epsilon_2 \sum_{k',b'} \rho_{kk'}^{bb'(2)}(0) (\mathbf{e}_2 \mathbf{d}_{k'g}^{b'a}) - i\epsilon_1 \sum_{k',b'} \rho_{kk'}^{bb'(2)}(\omega_2 - \omega_1) (\mathbf{e}_1 \mathbf{d}_{k'g}^{b'a}) + i\epsilon_2 \sum_a (\mathbf{e}_2 \mathbf{d}_{kg}^{ba'}) \rho_{gg}^{a'a(2)}(0) + i\epsilon_1 \sum_a (\mathbf{e}_1 \mathbf{d}_{kg}^{ba'}) \rho_{gg}^{a'a(2)}(\omega_2 - \omega_1) \quad (\text{A8})$$

The three terms in the r.h.s of eq A7 correspond to the CA', ESA1, and ESA2, respectively. The five terms in the r.h.s of eq A8 correspond to CA'', SE1, SE2, PB1, and PB2.

In the text, we separate the pump–probe dynamics into two contributions: (1) a sequential part  $\Delta A_s = \text{ESA1} + \text{SE1} + \text{PB1}$  and (2) a coherent part  $\Delta A_c = \text{ESA2} + \text{SE2} + \text{PB2} + \text{CA}' + \text{CA}''$ . The total pump–probe signal is  $\Delta A = \Delta A_s + \Delta A_c$ .

The elements of the Redfield tensor necessary to evaluate the relaxation terms in eqs A1–A8 are given in Appendix B.

## Appendix B

We consider a system–bath interaction in the form of eqs 5 and 6 with uniform (site-independent) oscillator displacement. Then the Redfield tensor elements needed to obtain the relaxation terms in eqs A1–A8 are the following (a, c denote vibronic sublevels of the ground-state g; b, d denote sublevels of the one-exciton states k, p, or s; f denotes sublevels of the two-exciton states q or r, and j is the number of vibrational modes):

$$\begin{aligned} R_{kgk'g}^{bab'a'} &= R_{kgk'g} + R_{bab'a'} & R_{kk'pp'}^{bb'dd'} &= R_{kk'pp'} + R_{bb'dd'} \\ R_{gggg}^{aa'cc'} &= R_{aa'cc'} & R_{qgq'g}^{fa'a'} &= R_{qgq'g} + R_{fa'a'} \\ R_{qkq'k'}^{fbr'b'} &= R_{qkq'k'} + R_{fbr'b'} \end{aligned} \quad (\text{B1})$$



$$\begin{aligned}
R_{k'g'g} &= \sum_{s,n} c_n^k c_n^{k'} (c_n^s)^2 J_{sk'} \quad |k\rangle = \sum_n c_n^k |n\rangle \\
R_{q'g'g} &= \sum_{\substack{r,n,n', \\ m>n, m'>n'}} c_{nm}^q c_{n'm'}^{q'} c_{nm}^r c_{n'm'}^r J_{rq'} (\delta_{nn'} + \delta_{nm'} + \\
&\quad \delta_{mn'} + \delta_{mm'}) \quad |q\rangle = \sum_{m>n} c_{nm}^q |n,m\rangle \\
R_{kk'pp'} &= \delta_{k'p'} R_{k'gpg} + \delta_{kp'} R_{k'gpg}^* - \sum_n c_n^k c_n^{k'} c_n^p (J_{kp} + J_{k'p}^*) \\
R_{qkq'k'} &= \delta_{kk'} R_{q'gq'g} + \delta_{qq'} R_{q'gq'g}^* - \\
&\quad \sum_{\substack{n,n', \\ m'>n'}} c_n^k c_n^{k'} c_{n'm'}^q c_{n'm'}^{q'} (J_{kk'}^* + J_{qq'}) (\delta_{nn'} + \delta_{nm'}) \quad (B2) \\
R_{bab'a'} &= \delta_{bb'} \sum_{j,a''} Q_{a'a''}^j Q_{a''a}^j \Psi_{a'a'}^j + \delta_{aa'} \sum_{j,b''} \tilde{Q}_{bb''}^j \tilde{Q}_{b''b}^j \Psi_{b'b'}^j \\
R_{bb'dd'} &= - \sum_j \tilde{Q}_{bd}^j \tilde{Q}_{b'd'}^j (\Psi_{bd}^j + \Psi_{b'd'}^j) + \\
&\quad \delta_{b'd'} \sum_{j,b''} \tilde{Q}_{bb''}^j \tilde{Q}_{b''d}^j \Psi_{b'd'}^j + \delta_{bd} \sum_{j,b''} \tilde{Q}_{b'b''}^j \tilde{Q}_{b''d'}^j \Psi_{b'd'}^j \\
R_{fafs'a'} &= R_{bab'a'} \{b \rightarrow f; \tilde{Q} \rightarrow \tilde{Q}\} \\
R_{aa'cc'} &= R_{bb'dd'} \{b \rightarrow a; d \rightarrow c; \tilde{Q} \rightarrow \tilde{Q}\} \\
R_{fd'f'd'} &= R_{bab'a'} \{b \rightarrow f; a \rightarrow d; \tilde{Q} \rightarrow \tilde{Q}; Q \rightarrow \tilde{Q}\} \quad (B3) \\
Q_{aa'}^j &= (\delta_{a'a-1} \sqrt{a} + \delta_{a'a+1} \sqrt{a+1}) / \sqrt{2} \\
\tilde{Q}_{bb'}^j &= \sum_{j,aa'} (Q^j - \Delta^j)_{aa'} \varphi_a^b \varphi_{a'}^{b'} = \\
&\quad (\delta_{b',b-1} \sqrt{b} + \delta_{b',b+1} \sqrt{b+1}) / \sqrt{2} \quad |b\rangle = \sum_a \varphi_a^b |a\rangle \\
\tilde{Q}_{ff'}^j &= \sum_{j,aa'} (Q^j - 2\Delta^j)_{aa'} \varphi_a^f \varphi_{a'}^{f'} = \\
&\quad (\delta_{f',f-1} \sqrt{f} + \delta_{f',f+1} \sqrt{f+1}) / \sqrt{2} \quad |f\rangle = \sum_a \varphi_a^f |a\rangle \quad (B4) \\
\Psi_{a'a''}^j &= \alpha^j \tau_c^j (1 + \exp(\omega_{a'a''}^j / k_B T))^{-1} \quad (B5)
\end{aligned}$$

$$J_{kk'} = (1 - \delta_{kk'}) \frac{\chi^2}{\omega_c} W^2 \exp(-W) (1 + \exp(\omega_{kk'} / k_B T))^{-1} + \delta_{kk'} \Gamma / 2$$

$$\chi = \sqrt{\beta} \quad W = \left| \frac{\omega_{kk'}}{\omega_c} \right| \quad (B6)$$

The vibrational Redfield tensor is expressed through the matrix elements of the vibrational coordinate  $Q^j$  in the eigenstate basis and the spectral density function  $\Psi_{a'a'}^j$  that is proportional to the mean square of the fluctuation amplitude  $\alpha^j$  (see eq 6a) and to the correlation time  $\tau_c^j$ , reflecting the spectral density of fluctuations at frequency  $\omega_{a'a'}^j = \pm \Omega^j$  (for one-phonon relaxation). The exciton Redfield tensor contains the wave function amplitudes  $c_n^k$  and  $c_{nm}^q$  connecting the site and exciton (eigenstate) representation and spectral density function  $J_{kk'}$ . The latter includes the coupling parameter (i.e., the amplitude of the bath-

induced fluctuations)  $\chi$  related to the mean square of the fluctuation amplitude  $\beta$  (see eq 6b) and their spectral density at frequency  $\omega_{kk'}$ .  $\Gamma$  is the pure dephasing parameter. In eq B6, the spectral density was taken in the simplest form (i.e.,  $W^2 \exp(-W)$ ). This phenomenological spectral density can be replaced by more complicated functions if one specifies the bath properties. For example, the  $J_{kk'}$  functions can be calculated using the Brownian oscillator spectral density for the collective bath coordinates.<sup>24,43</sup> In our model, the system–bath interactions are uncorrelated for different sites and are site-independent (eqs 5 and 6) (i.e., each chromophore interacts with its own bath). Modeling this bath by a single overdamped Brownian oscillator with spectral density

$$C(\omega) = 2\lambda \frac{\Lambda \omega}{\Lambda^2 + \omega^2} \quad (B7)$$

( $\lambda$  is coupling constant,  $\Lambda^{-1}$  is the relaxation time) and using the results of ref 43, we get

$$\begin{aligned}
J_{kk'} &= \\
&- \lambda \Lambda \left( \frac{\cot(\Lambda/2k_B T) - i}{\Lambda + i\omega_{kk'}} + 4k_B T \sum_{n=1}^{\infty} \frac{\nu_n}{\nu_n^2 - \Lambda^2} \frac{1}{\nu_n + i\omega_{kk'}} \right) \\
&\nu_n = 2\pi n k_B T \quad (B8)
\end{aligned}$$

## Appendix C

If **a**, **b**, **c**, **d** are arbitrary vectors (different dipole moments in eqs 3 and A1–A8), then we have to average their projections on the field polarizations **e**<sub>1</sub> and **e**<sub>2</sub> according to the following rules:

$$\begin{aligned}
(\mathbf{e}_1 \mathbf{a})(\mathbf{e}_1 \mathbf{b})(\mathbf{e}_2^\parallel \mathbf{c})(\mathbf{e}_2^\parallel \mathbf{d}) &= \frac{1}{15} [(\mathbf{ab})(\mathbf{cd}) + (\mathbf{ac})(\mathbf{bd}) + (\mathbf{ad})(\mathbf{bc})] \\
(\mathbf{e}_1 \mathbf{a})(\mathbf{e}_1 \mathbf{b})(\mathbf{e}_2^\perp \mathbf{c})(\mathbf{e}_2^\perp \mathbf{d}) &= \frac{1}{30} [4(\mathbf{ab})(\mathbf{cd}) - (\mathbf{ac})(\mathbf{bd}) - \\
&\quad (\mathbf{ad})(\mathbf{bc})] \\
(\mathbf{e}_1 \mathbf{a})(\mathbf{e}_1 \mathbf{b})(\mathbf{e}_2^m \mathbf{c})(\mathbf{e}_2^m \mathbf{d}) &= \frac{1}{9} [(\mathbf{ab})(\mathbf{cd})] \\
\mathbf{e}_2^m &= \sqrt{3}(\mathbf{e}_2^\parallel + \sqrt{2}\mathbf{e}_2^\perp) \quad (C1)
\end{aligned}$$

The indexes  $\parallel$ ,  $\perp$ , and  $m$  correspond to the parallel, perpendicular, and magic angle orientations, respectively, of the probe.

## References and Notes

- (1) van Grondelle, R.; Dekker, J. P.; Gillbro, T.; Sundström, V. *Biochim. Biophys. Acta* **1994**, *1187*, 1.
- (2) Van Amerongen, H.; Valkunas, L.; van Grondelle, R. *Photosynthetic Excitons*; World Scientific: River Edge, NJ, 2000.
- (3) McDermott, G.; Prince, S. M.; Freer, A. A.; Hawthornthwaite-Lawless, A. M.; Papiz, M. Z.; Cogdell, R. J.; Isaacs, N. W. *Nature (London)* **1995**, *374*, 517.
- (4) Koepke, J.; Hu, X.; Muenke, C.; Schulten, K.; Michel, H. *Structure* **1996**, *4*, 581.
- (5) Sundström, V.; Pullerits, T.; van Grondelle, R. *J. Phys. Chem. B* **1999**, *103*, 2327.
- (6) Xiao, W.; Lin, S.; Taguchi, A. K. W.; Woodbury, N. W. *Biochemistry* **1994**, *33*, 8313.
- (7) Visser, H. M.; Somsen, O. J. G.; van Mourik, F.; Lin, S.; van Stokkum, I. H. M.; van Grondelle, R. *Biophys. J.* **1995**, *69*, 1083.
- (8) Visser, H. M.; Somsen, O. J. G.; van Mourik, F.; van Grondelle, R. *J. Phys. Chem.* **1996**, *100*, 18859.
- (9) Nagarajan, V.; Alden, R. G.; Williams, J. C.; Parson, W. W. *Proc. Natl. Acad. Sci. U.S.A.* **1996**, *93*, 13774.
- (10) Nagarajan, V.; Johnson, E. T.; Williams, J. C.; Parson, W. W. *J. Phys. Chem. B* **1999**, *103*, 2297.
- (11) Savikhin, S.; Struve, W. S. *Chem. Phys.* **1996**, *210*, 91.

- (12) Kennis, J. T. M.; Streltsov, A. M.; Vulto, S. I. E.; Aartsma, T. J.; Nozava, T.; Amesz, J. *J. Phys. Chem. B* **1997**, *101*, 7827.
- (13) Kennis, J. T. M.; Streltsov, A. M.; Permentier, H.; Aartsma, T. J.; Amesz, J. *J. Phys. Chem. B* **1997**, *101*, 8369.
- (14) Chachisvilis, M.; Kühn, O.; Pullerits, T.; Sundström, V. *J. Phys. Chem. B* **1997**, *101*, 7275.
- (15) Monshouwer, R.; Baltuška, A.; van Mourik, F.; van Grondelle, R. *J. Phys. Chem. A* **1998**, *102*, 4360.
- (16) Vulto, S. I. E.; Kennis, J. T. M.; Streltsov, A. M.; Amesz, J.; Aartsma, T. J. *J. Phys. Chem. B* **1999**, *103*, 878.
- (17) Polívka, T.; Pullerits, T.; Herek, J. L.; Sundström, V. *J. Phys. Chem. B* **2000**, *104*, 1088.
- (18) Book, L. D.; Ostafin, A. E.; Ponomarenko, N.; Norris, J. R.; Scherer, N. F. *J. Phys. Chem. B* **2000**, *104*, 8295.
- (19) van Mourik, F.; Hawthornthwaite, A. M.; Vonk, C.; Evans, M. B.; Cogdell, R. J.; Sundström, V.; van Grondelle, R. *Biochim. Biophys. Acta* **1992**, *1140*, 85.
- (20) van Mourik, F.; Visschers, R. W.; van Grondelle, R. *Chem. Phys. Lett.* **1992**, *193*, 1.
- (21) Monshouwer, R.; Visschers, R. W.; van Mourik, F.; Freiberg, A.; van Grondelle, R. *Biochim. Biophys. Acta* **1995**, *1229*, 373.
- (22) Novoderezhkin, V.; Monshouwer, R.; van Grondelle, R. *J. Phys. Chem. B* **2000**, *104*, 12056.
- (23) Redfield, A. G. *Adv. Magn. Reson.* **1965**, *1*, 1.
- (24) Mukamel, S. *Principles of Nonlinear Optical Spectroscopy*; Oxford University Press: New York, 1995.
- (25) Pollard, W. T.; Felts, A. K.; Friesner, R. A. *Adv. Chem. Phys.* **1996**, *93*, 77.
- (26) Novoderezhkin, V.; Monshouwer, R.; van Grondelle, R. *Biophys. J.* **1999**, *77*, 666.
- (27) Koolhaas, M. H. C.; van der Zwan, G.; Frese, R. N.; van Grondelle, R. *J. Phys. Chem. B* **1997**, *101*, 7262.
- (28) Koolhaas, M. H. C.; Frese, R. N.; Fowler, G. J. S.; Bibby, T. S.; Georgakopoulou, S.; van der Zwan, G.; Hunter, C. N.; van Grondelle, R. *Biochemistry* **1998**, *37*, 4693.
- (29) Kühn, O.; Sundström, V. *J. Chem. Phys.* **1997**, *107*, 4154.
- (30) Jean, J. M.; Fleming, G. R. *J. Chem. Phys.* **1995**, *103*, 2092.
- (31) Kühn, O.; Sundström, V. *J. Phys. Chem. B* **1997**, *101*, 3432.
- (32) Kumble, R.; Palese, S.; Visschers, R. W.; Dutton, P. L.; Hochstrasser, R. M. *Chem. Phys. Lett.* **1996**, *261*, 396.
- (33) Monshouwer, R. The Nature and Dynamics of Excitations in Photosynthetic Light-Harvesting. Ph.D. Thesis, Vrije Universiteit, Amsterdam, The Netherlands, 1998.
- (34) van Oijen, A. M.; Ketelaars, M.; Köhler, J.; Aartsma, T. J.; Schmidt, J. *Science (Washington, D.C.)* **1999**, *285*, 400.
- (35) Ketelaars, M.; van Oijen, A. M.; Matsushita, M.; Köhler, J.; Schmidt, J.; Aartsma, T. J. *Biophys. J.* **2001**, *80*, 1591.
- (36) Matsushita, M.; Ketelaars, M.; van Oijen, A. M.; Köhler, J.; Aartsma, T. J.; Schmidt, J. *Biophys. J.* **2001**, *80*, 1604.
- (37) Wendling, M.; Lapouge, K.; van Mourik, F.; Novoderezhkin, V.; Robert, B.; van Grondelle, R., submitted for publication.
- (38) Novoderezhkin, V.; Monshouwer, R.; van Grondelle, R. *J. Phys. Chem. B* **1999**, *103*, 10540.
- (39) Joo, T.; Jia, Y.; Yu, J.-Y.; Jonas, D. M.; Fleming, G. R. *J. Phys. Chem.* **1996**, *100*, 2399.
- (40) Jimenez, R.; van Mourik, F.; Yu, J. Y.; Fleming, G. R. *J. Phys. Chem. B* **1997**, *101*, 7350.
- (41) Salverda, J. M.; van Mourik, F.; van der Zwan, G.; van Grondelle, R. *J. Phys. Chem. B* **2000**, *104*, 11395.
- (42) Arnett, D. C.; Moser, C. C.; Dutton, P. L.; Scherer, N. F. *J. Phys. Chem. B* **1999**, *103*, 2014.
- (43) Dahlbom, M.; Minami, T.; Chernyak, V.; Pullerits, T.; Sundström, V.; Mukamel, S. *J. Phys. Chem. B* **2000**, *104*, 3976.
- (44) Meier, T.; Chernyak, V.; Mukamel, S. *J. Phys. Chem. B* **1997**, *101*, 7332.
- (45) Reddy, N. R. S.; Picorel, R.; Small, G. J. *J. Phys. Chem.* **1992**, *96*, 6458.